



Burst Phase Distribution of SGR J1935+2154 Based on Insight-HXMT

Xue-Feng Lu^{1,2} , Li-Ming Song^{1,2} , Ming-Yu Ge¹, You-Li Tuo¹ , Shuang-Nan Zhang^{1,2}, Jin-Lu Qu¹, Ce Cai³,
Sheng-Lun Xie^{1,4}, Cong-Zhan Liu¹, Cheng-Kui Li¹, Yu-Cong Fu¹, Ying-Chen Xu^{1,2}, and Tian-Ming Li^{1,2}

¹Key Laboratory of Particle Astrophysics, Institute of High Energy Physics, Beijing 100049, China; luxf@ihep.ac.cn

²University of Chinese Academy of Sciences, Chinese Academy of Sciences, Beijing 100049, China

³College of Physics and Hebei Key Laboratory of Photophysics Research and Application, Hebei Normal University, Shijiazhuang 050024, China

⁴Institute of Astrophysics, Central China Normal University, Wuhan 430079, China

Received 2022 October 20; revised 2022 December 25; accepted 2023 January 3; published 2023 February 28

Abstract

On 2020 April 27, the soft gamma-ray repeater SGR J1935+2154 entered its intense outburst episode again. Insight-HXMT carried out about one month observation of the source. A total number of 75 bursts were detected during this activity episode by Insight-HXMT, and persistent emission data were also accumulated. We report on the spin period search result and the phase distribution of burst start times and burst photon arrival times of the Insight-HXMT high energy detectors and Fermi/Gamma-ray Burst Monitor (GBM). We find that the distribution of burst start times is uniform within its spin phase for both Insight-HXMT and Fermi/GBM observations, whereas the phase distribution of burst photons is related to the type of a burst's energy spectrum. The bursts with the same spectrum have different distribution characteristics in the initial and decay episodes for the activity of magnetar SGR J1935+2154.

Key words: physical data and processes – radiation: dynamics – radiation mechanisms: general

1. Introduction

Magnetars are a class of special celestial objects with super strong magnetic fields (often more than 10^{14} G) in the universe, which are usually thought of as young neutron stars. Compared to conventional pulsars, magnetars are characterized by intense energetic phenomena in the X-ray band and the soft gamma-ray band (Kaspi & Beloborodov 2017). This is why magnetars are commonly classified as anomalous X-ray pulsars (AXPs) and soft gamma repeaters (SGRs) (Woods et al. 2008; Scholz & Kaspi 2011). It is widely believed that magnetars are powered by the decay of their supercritical magnetic fields, perhaps an external magnetic field (Kouveliotou et al. 1998) or an internal magnetic field (Thompson & Duncan 1995).

SGR J1935+2154 was discovered in 2014 when Swift-BAT (Burst Alert Telescope) was triggered by short bursts from Galactic plane (Stamatikos et al. 2014). Subsequent Chandra observations located the burst from the direction of the supernova remnant G57.2+0.8 (Kothes et al. 2018). Based on Chandra and XMM-Newton data, a spin period of 3.24 s and spin-down rate of $1.43(1) \times 10^{-11} \text{ s s}^{-1}$ was discovered, which implying a surface bipolar magnetic field strength of approximately 2.2×10^{14} G (Israel et al. 2016). Combined with its burst characteristics, the source was identified as a magnetar. In 2015, 2016 and 2019, SGR J1935+2154 has many burst activity episodes, releasing a lot of energy in persistent and burst emission (Younes et al. 2017; Lin et al. 2020b).

Since 2020 April 27, SGR J1935+2154 entered into its active episode again, and multiple X-ray and gamma-ray

telescopes detected a large number of intense bursts. Several hours after the outburst onset, CHIME known as Canadian Hydrogen Intensity Mapping Experiment (CHIME/FRB Collaboration et al. 2020) and STARE2 known as The Survey for Transient Astronomical Radio Emission 2 (Bochenek et al. 2020) detected an intense fast radio burst (FRB) from the source direction, respectively. At the same time, multiple hard X-ray telescopes (Mereghetti et al. 2020; Li et al. 2021; Ridnaia et al. 2021; Younes et al. 2021) detected the hard X-ray signal from the source that was associated with this FRB. The correlation between X-ray bursts and FRBs provides evidence that at least some FRBs can originate from magnetars. After initial 2020 active episode, NICER, Fermi and Insight-HXMT performed long-term observations of the source evolution. (Younes et al. 2020) presented observations of a burst storm and long-term persistent emission evolution of SGR J1935+2154 based on NICER data. They find a double-peaked pulse profile of soft X-ray emission of the source, corresponding to a frequency $f=0.307946(2)$ Hz. The burst peak arrival times detected by NICER in 1–10 keV follow a uniform distribution in pulse profile. (Kaneko et al. 2021) presented the results of time-resolved spectral analysis of the “burst forest” lasted for 130 s observed by Fermi/Gamma-ray Burst Monitor (GBM). They converted the GBM photon arrival times to barycentric times and studied the lightcurve and the spectral parameter evolution with the NICER pulse profile. The results show that the Comptonized model (COMPT, a power law with an exponential cutoff) fits these bursts with an anti-correlation,

i.e., the spectra with high peak energy E_{peak} appear at or close to the minima of the pulse profile. They also noted that even though the flux varied by two orders of magnitude the single blackbody kT remains constant around 7 keV and the double blackbodies high kT also remains roughly constant at about 14 keV. In (Lin et al. 2020a), temporal and time-integrated analysis of the 125 bursts (excluding the 130 s burst forest) of SGR J1935+2154 2020 active episode detected by Fermi/GBM was reported. They found a growing trend for the evolution of the total burst fluence since its discovery in all active episodes. They also studied the last time evolution of the burst, finding a similar log-Gaussian distribution as other magnetars.

On April 28, approximately 13 hr after the outburst episode onset, Insight-HXMT started observation of this source. This observation lasted 33 days, and a total number of 75 bursts were detected. In (Cai et al. 2022b), they reported similar results as (Lin et al. 2020a) for these 75 bursts, which are on average much fainter than the GBM bursts reported in (Lin et al. 2020a). In this paper, we study on the burst phase evolution properties of Fermi/GBM 125 bursts and Insight-HXMT 75 bursts, and also the 2020 persistent emission based on Insight-HXMT data. Section 2 gives the HXMT data reduction methods, Section 3 gives the analysis results, and Section 4 presents the discussion.

2. Observation and Data Reduction

Insight-HXMT was launched on 2017 June 15, which carries three collimated telescopes covering 1–10 keV (the Low Energy X-ray telescope, LE, geometrical area of 384 cm²), 5–30 keV (the Medium Energy X-ray telescope, ME, geometrical area of 952 cm²) and 20–250 keV (the High Energy X-ray telescope, HE, geometrical area of about 5000 cm²) (Cao et al. 2020; Chen et al. 2020; Liu et al. 2020; Zhang et al. 2020). The Target of Opportunity (ToO) observation for Insight-HXMT of SGR J1935+2154 lasted from April 28 07:14:51 UTC to June 1 00:00:01 UTC with a total effective exposure of 1650 ks. The detailed observation time list can be found in (Cai et al. 2022a). We refined the Insight-HXMT burst information with the same data reduction method as shown in (Cai et al. 2022a). For Fermi/GBM we used the same data reduction and burst refining method as shown in (Lin et al. 2020a). For phase analysis, all the burst data have been converted to barycentric times.

The event data are processed with the Insight-HXMT Data Analysis Software package (HXMTDAS) version 2.05. Standard data processing is used for HE, ME and LE event data. First hepical, mepical and lepical are used to calibrate event photons of HE, ME and LE, respectively, with Calibration Database (CALDB) of Insight-HXMT. Then good time interval is done directly for HE calibrated data with hegtigen. For LE data with the two-split events reconstruction

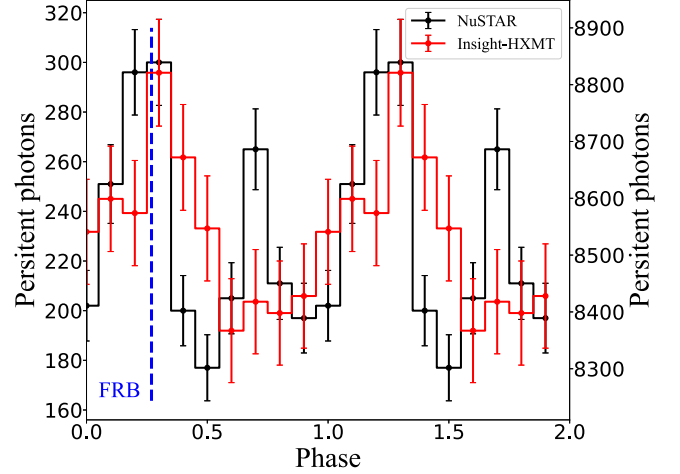


Figure 1. Comparing the persistent X-ray pulse profile of Insight-HXMT with NuSTAR, using the search period $f = 0.3079452$ Hz ($T_0 = 58967.423047$ MJD) of NuSTAR on May 2, the data of Insight-HXMT is used from May 1 to 5 in the energy range 1.5–6.8 keV. The black line is the NuSTAR 1.0–6.0 keV result, and the red line is the Insight-HXMT result. The blue dashed vertical line represent the phase of FRB 200428. The left axis is the NuSTAR scale, and the right axis is the Insight-HXMT scale.

and classification are executed with lerecon first and then legtigen. For ME data, megrade is used to calculate event grade and dead time correction before megtigen. Finally, hescreen, mecreen and lescreen are used to do good time data extraction and hxbary is used to do solar system centroid correction for subsequent phase analysis. Then all the burst signals and spurious pulse signals are thoroughly removed to do spin period search. Based on NuSTAR (Borghese et al. 2020) and NICER (Younes et al. 2020) results, SGR J1935+2154 persistent emission mainly concentrated in the low energy range, thus the X-ray pulse profile analysis of the source only use the Insight-HXMT LE data.

3. Result

3.1. X-Ray Pulse Profile Analysis Based on Insight-HXMT LE Data

To check Insight-HXMT detection ability for the persistent emission of SGR J1935+2154, we performed a preliminary examination of the low-energy data from 1.5–6.8 keV of Insight-HXMT based on the periodic search results $f = 0.3079452$ Hz ($T_0 = 58967.423047$ MJD) on 2020 May 2 of NuSTAR observations reported in (Borghese et al. 2020). With the Insight-HXMT LE data from May 1 to 5, we folded the pulse profile and found that Insight-HXMT could give similar pulse profiles under the periodic parameters given by NuSTAR, as shown in Figure 1, where the red line represents the Insight-HXMT result, whereas the black line represents the NuSTAR result. FRB 200428 phase is also marked in the figure

with the blue dashed line. We can see that Insight-HXMT does detect persistent radiation photons from the magnetar SGR J1935+2154 during its observations. We also find that the pulse profile observed by Insight-HXMT shows a slight deviation compared to NuSTAR, which may be due to the long time span of the Insight-HXMT data and possible evolution of the period, and mainly due to the low signal to noise ratio of Insight-HXMT LE data, as shown in the figure's right scale, Insight-HXMT has a very high background and this will cause large fluctuations in the profile.

Subsequently, we carried out a detailed study on the one month observation data of Insight-HXMT, and searched the spin period of SGR J1935+2154 based on Insight-HXMT LE data. Considering the rapid evolution of magnetar spin period and the fluence decay of the persistent radiation after the burst episode onset, we grouped the data of Insight-HXMT. Finally, we found the periodic signal in the data segment MJD 58969.29054398 to MJD 58972.22856481. We restricted our search interval to the frequency range $0.3079 \text{ Hz} < f < 0.3080 \text{ Hz}$, which covers the source spin frequency $f = 0.3079462 \text{ Hz}$ reported in (Younes et al. 2020) with NICER data. We found the largest χ^2 value of 33.2 (corresponding to the largest $Z_1^2 = 30.2$, Z^2 is conceptually similar to the χ^2 but has high values when the signal is well described by a small number of sinusoidal harmonics, the specific expression can be found in Buccheri et al. 1983) at frequency $f = 0.3079433(14) \text{ Hz}$, which corresponds to a spin period of $3.24735(2) \text{ s}$.

Due to the large margin of error, here we just give a simple result of Insight-HXMT pulse period search. Also because the long time span of our study, none of the existing ephemeris can fully cover all the bursts. The ephemeris used in this paper is fitted results based on the combined ephemeris evolution data derived from NuSTAR, NICER and XMM-Newton in (Ge et al. 2022), which yield $f = 0.30794447(1) \text{ Hz}$, $\dot{f} = -2.165 \times 10^{-12} \text{ Hz s}^{-1}$ at an epoch $T_0 = 58967 \text{ MJD}$; this ephemeris can cover the whole observation period of Insight-HXMT, and is used in the subsequent study of the burst phase distribution for the bursts detected with Fermi/GBM and Insight-HXMT.

3.2. Burst Phase Characteristics

During Insight-HXMT 33 days observation of SGR J1935+2154, only 61 bursts are detected by LE telescope, and most of them are very weak with only several photons. But for HE telescope there are 75 remarkable bursts, while for ME telescope there are 74 bursts. Because HE has more complete samples, and LE and ME burst photons have consistent statistical characteristics as HE, we only use HE burst data in the subsequent analysis. Since the energy spectra and flux information about the bursts have been reported in (Cai et al. 2022b), this work mainly analyzes the phase distribution characteristics of these bursts. In the paper, the burst start time is defined as the start time of the first Bayesian block

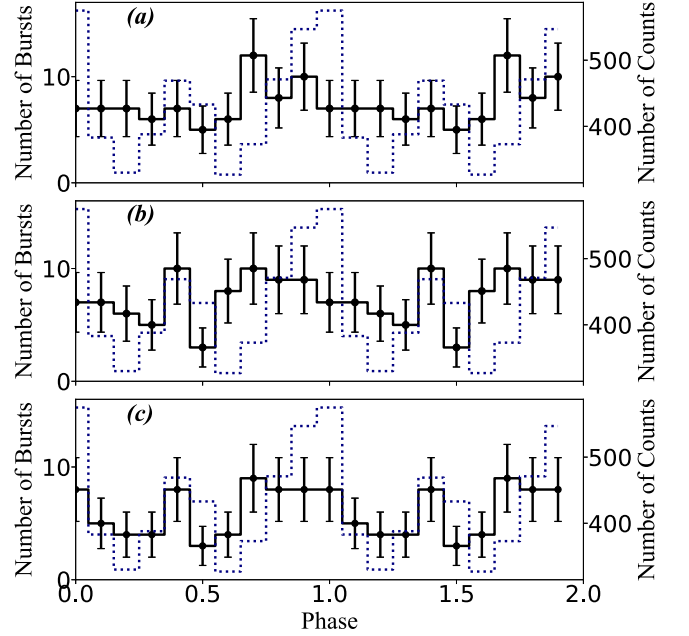


Figure 2. The phase distribution of the burst start times. (a) The HXMT HE telescope data, (b) the HXMT ME telescope data, and (c) the HXMT LE data. In each panel, the black solid curve is HXMT data, the dotted light blue curve is the X-ray pulse profile conducted with NuSTAR 2020 May 2 data.

(Scargle et al. 2013) within the burst time window. First, a statistical analysis of the start time for each Insight-HXMT telescope burst is performed, as shown in Figure 2, where panel (a) shows HE bursts, panel (b) shows ME bursts and panel (c) shows LE bursts, the burst start times for the three telescopes of Insight-HXMT follow the same distribution; the χ^2 test is used to check any structure significance, but no significant difference is found from a uniform distribution (with equivalent Gaussian significance less than 1σ).

According to Lin et al. (2020a) and our search result, during the 2020 April activity episode of SGR J1935+2154, Fermi/Gamma-ray Burst Monitor found a total number of 125 bursts (from April 27 to May 20, excluding the 130s “burst forest”). The 12 bursts from April 28 06:00:00 UTC to May 20 are excluded from these 125 bursts, and the rest 113 bursts are used to compare with Insight-HXMT observations; the Fermi/GBM burst episode here is deemed as an intense activity stage. For comparison, the bursts period of Insight-HXMT observation is called the decay activity stage. Thus we have a complete separation of Fermi/GBM and Insight-HXMT bursts in time. The start time of each burst and the photon arrival times within the burst are converted to barycentric time and then phase. The burst start time distribution in phase for the two stages is shown in Figure 3. The top panel shows the start time distribution of the 75 bursts detected with Insight-HXMT HE, and the bottom panel shows the start time distribution of the 113 bursts detected with Fermi/GBM. The dotted light blue line is the

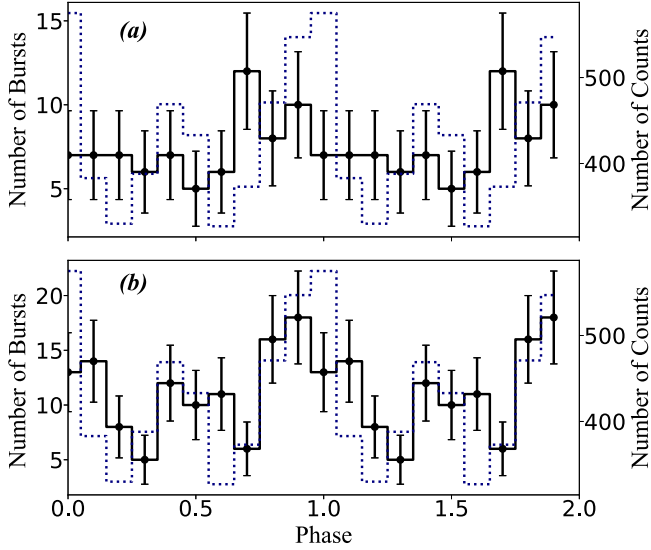


Figure 3. The distribution of burst start time in phase space for Fermi/GBM and Insight-HXMT. (a) All 75 bursts start time of Insight-HXMT, and (b) is for the 113 bursts start time of Fermi. The solid black line is the burst numbers, and the dotted light blue line is the X-ray pulse profile with the NuSTAR May 2 data.

X-ray pulse profile based on NuSTAR May 2 data. After χ^2 test, neither Fermi/GBM nor Insight-HXMT detected any significant structure in phase distribution (with equivalent Gaussian significance less than 2σ).

The energy spectrum of magnetar bursts is complex and diverse, and different types of bursts may show unique distribution characteristics in phase due to different generating mechanisms. To study the phase distribution characteristics of burst photons with different types of energy spectrum, we classify the bursts according to the energy spectrum fitting model actually used by Insight-HXMT and Fermi/GBM. In the energy spectrum fitting analysis of the Insight-HXMT's 75 bursts, the cut off power law (CPL), double blackbodies (BB+BB), blackbody plus power law (BB+PL), single blackbody (BB) and power law (PL) fitting models are used; the phase distribution of burst photon arrival time for each type model is investigated respectively. The result is shown in Figure 4, where panel (a) shows bursts with BB spectra, panel (b) shows bursts with BB+BB spectra, panel (c) shows bursts with BB+PL spectra, panel (d) shows bursts with CPL spectra, and panel (e) shows bursts with PL spectra. For each panel, the black solid line represents burst photon number, and the dotted light blue line is the X-ray pulse profile of SGR J1935+2154 based on NuSTAR May 2 observation. We find that the phase distribution of burst photons with power law spectrum component showed a tendency to align with the main peak of the persistent radiation profile, especially the single PL spectrum feature is the most obvious, almost all the burst photons are concentrated to the main peak. For bursts with BB

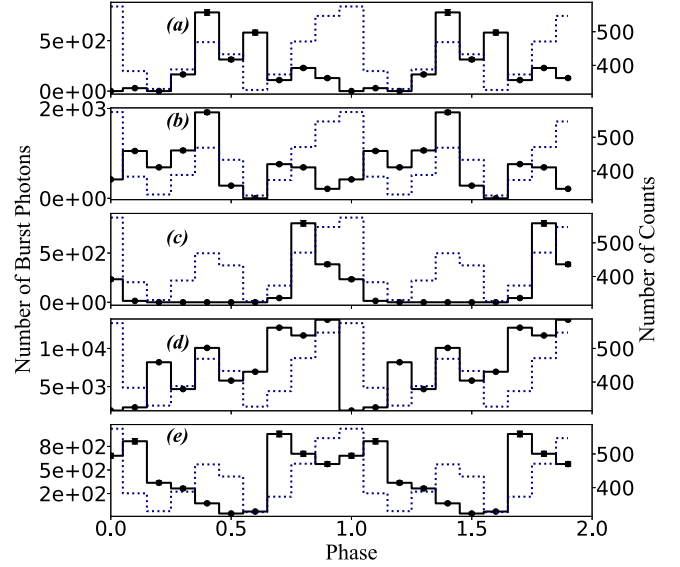


Figure 4. The phase distribution of Insight-HXMT burst photons for different spectra models. (a) Bursts with BB spectra, (b) is for bursts with BB+BB spectra, (c) is for bursts with BB+PL spectra, (d) is for bursts with CPL spectra, and (e) is for bursts with PL spectra. For each panel, the black solid line represents burst photon numbers, while the dotted lightblue line is the X-ray pulse profile of SGR J1935+2154 based on NuSTAR May 2 observation.

spectrum their burst photons tend to synchronize with the secondary peak, especially the single BB bursts. For BB+PL burst photons, their characteristics are dominated by the single PL feature, which means the phase distribution of burst photon arrival time is synchronized with the main persistent peak.

In (Lin et al. 2020a), the bursts spectra observed by Fermi/GBM have fitting models of power law, cut off power law, optically thin thermal bremsstrahlung (OTTB), single blackbody and double blackbodies. Some bursts can be clarified by the spectrum type, and there are also a large amount of bursts which can be fitted either by CPL or BB+BB. The numbers of each type of bursts for the Insight-HXMT and Fermi-GBM are shown in Table 1. Here we choose the common model PL, BB and BB+BB to compare for the Insight-HXMT and Fermi/GBM burst properties. As we can see in Figures 5–7, for both PL and BB bursts, Fermi/GBM observed a relatively small number, and there is no significant structure in the distribution of the burst start times of these two types. But for burst photon arrival time, Fermi/GBM BB burst photons are obviously concentrated in the transition valley from the main peak to the secondary peak, while for Insight-HXMT bursts there are almost no photons in the same phase. Fermi/GBM PL burst photons are basically synchronized with the persistent phase profile, showing a double-peak structure, the same PL bursts for Insight-HXMT shown a similar distribution with all the photons concentrated to the same position of the persistent

Table 1
Number of Bursts of Different Spectrum Types

| Telescope | BB | BB+BB | BB+PL | PL | CPL | CPL\BB+BB ^a | OTTB ^b | Total Number |
|--------------|----|-------|-------|----|-----|------------------------|-------------------|--------------|
| Insight-HXMT | 13 | 13 | 3 | 22 | 24 | 0 | 0 | 75 |
| Fermi/GBM | 4 | 29 | 0 | 9 | 4 | 39 | 26 | 113 |

Notes.

^a For Fermi/GBM there are 39 bursts whose spectra can be perfectly fitted with both CPL and BB+BB.

^b OTTB is optically thin thermal bremsstrahlung.

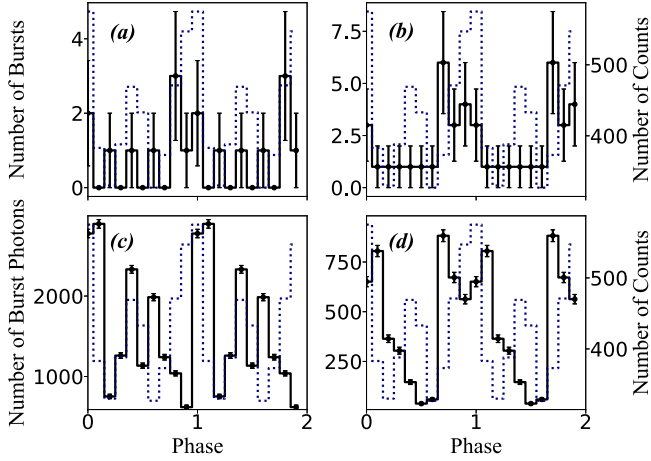


Figure 5. The burst start time and photon arrival time distribution in phase of Fermi/GBM and Insight-HXMT power law bursts. Left: Fermi/GBM 20–200 keV data, right: Insight-HXMT 20–200 keV data. (a), (b) Burst start time, where the solid black curve is for burst number; (c), (d) burst photon arrival time, where the solid black curve is for burst photon number. In each panel the dotted light blue curve is the X-ray pulse profile based on NuSTAR May 2 observation. All of the times have been converted to barycentric time and then phase.

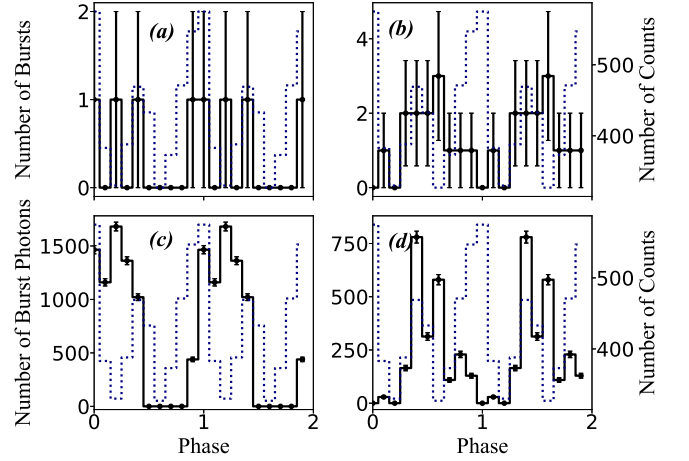


Figure 6. The burst start time and photon arrival time distribution in phase of Fermi/GBM and Insight-HXMT for BB bursts. Left: Fermi/GBM 20–200 keV data, right: Insight-HXMT 20–200 keV data. (a), (b) Burst start time, where the solid black curve is for burst numbers; (c), (d) burst photon arrival time, where the solid black curve is for burst photon numbers. In each panel the dotted light blue curve is the X-ray pulse profile based on NuSTAR May 2 observation. All of the times have been converted to barycentric time and then phase.

main peak. The burst photons of Fermi/GBM BB+BB burst distribute in the same position as the main peak, whereas Insight-HXMT bursts have few photons in the same position. No significant distribution characteristics are found for the burst start time of either spectrum type burst.

In summary, at the intense activity stage of the magnetar SGR J1935+2154 outburst (shown by Fermi/GBM observation), there is an obvious double-peak structure in the phase of PL burst photons. As the magnetar enters the activity decay stage (shown by Insight-HXMT observation), almost all of the power law photons concentrate near the main peak. However, the blackbody and double-blackbody burst photons have an obvious concentrated distribution at the beginning of the magnetar activity, yet in the decay episode of magnetar activity, the photon distribution characteristics are weakened, but there is still an obvious change in phase compared with the initial stage.

3.3. Hardness Ratio of Burst Photons

We studied the hardness ratio distribution of the high-energy versus the medium-energy of Insight-HXMT for all the bursts. The result is shown in Figure 8, where the solid black curve is for the hardness ratio, and the dotted light blue curve is for SGR J1935+2154 X-ray pulse profile conducted from NuSTAR May 2 data. The hardness ratio curve has a significant double-peak structure, where the valley position coincides with the X-ray pulse profile minimum point, while the peak position has an offset compared to the two peaks.

4. Discussion

According to the above analysis results, we did not find a precise spin period from Insight-HXMT observation data due to the bad Signal To Noise Ratio. The start time distribution of bursts in phase shows a uniform property. The energy spectrum of SGR J1935+2154 observed by Fermi/GBM and Insight-HXMT at its intense activity stage after outbreak is complex,

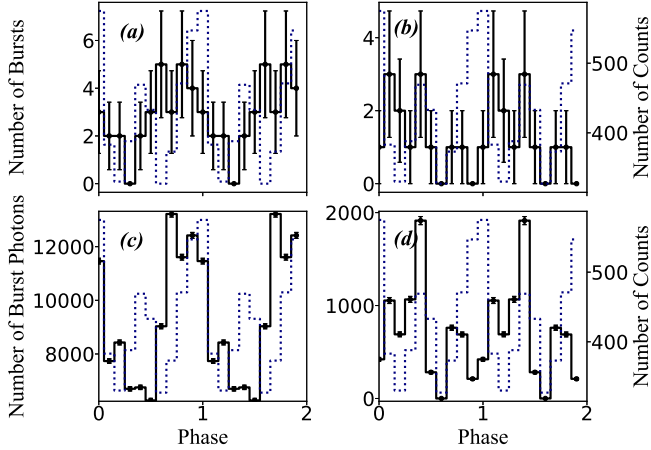


Figure 7. The burst start time and photon arrival time distribution in phase of Fermi/GBM and Insight-HXMT for BB+BB bursts. Left: Fermi/GBM 20–200 keV data, right: Insight-HXMT 20–200 keV data. (a), (b) Burst start time, where the solid black curve is for burst number; (c), (d) burst photon arrival time, where the solid black curve is for burst photon number. In each panel the dotted light blue curve is the X-ray pulse profile based on NuSTAR May 2 observation. All of the times have been converted to barycentric time and then phase.

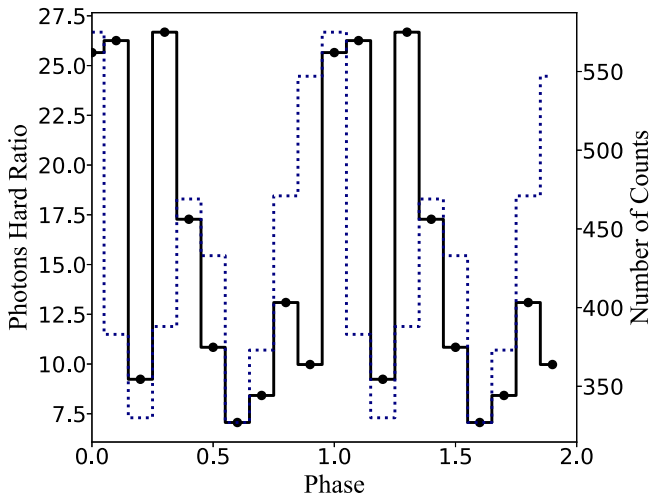


Figure 8. The hardness ratio of the high energy 30–250 keV to the medium energy 10–30 keV of the Insight-HXMT bursts. The solid black curve is for the hardness ratio, where the dotted light blue curve is for SGR J1935+2154 X-ray pulse profile conducted from NuSTAR May 2 data.

mainly double blackbody spectrum and power law spectrum. In the phase space, the burst photons mainly come from the region corresponding to the two peaks of the persistent X-ray pulse profile. During the decay stage of the magnetar, corresponding to bursts detected by Insight-HXMT, the burst photon distribution with the same spectrum type has obvious shift in phase relative to the intense stage of the outburst.

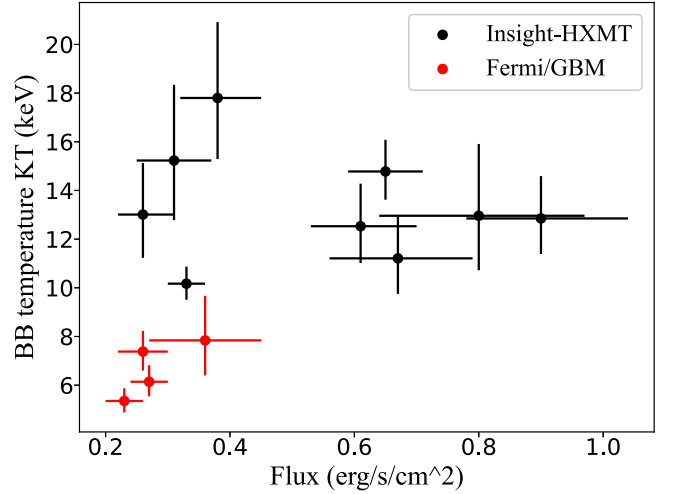


Figure 9. The relationship between temperature and flux of blackbody spectrum bursts, red dots represent Fermi/GBM bursts, all of which are during the activity period on April 27, and black dots are Insight-HXMT data, all of which are after April 28.

We analyzed the variation characteristics of burst temperature with flux for Fermi/GBM and Insight-HXMT single blackbody spectrum type, and the results are shown in Figure 9, where the black dots are Insight-HXMT BB bursts, and the red dots are Fermi/GBM bursts. It can be seen that the temperature of both Fermi/GBM and Insight-HXMT blackbody spectra does not evolve with the flux dramatically. It can also be seen that the surface temperature for region producing single blackbody spectrum burst at the beginning of the outburst is relatively low compared to which the outbreak enters the decreasing stage, which is consistent with the distribution trend of the burst photons shown in Figure 6, where the burst photons concentrated near the valley of the pulse profile at the initial stage but second maximum at the decay stage.

Although we did not find any significant structural features in the phase distribution of the burst start times, we found a tendency that the burst start times may align with the maxima peak of the X-ray pulse profile under certain conditions, such as the Fermi/GBM observations at the beginning of the outburst (see Figure 3(b)), and the bursts with power law spectrum at different outburst activity stages (see Figure 5), and also the bursts with double BB spectrum (see Figure 7). In addition to this tendency of the burst start times, the photon arrival times of each burst have a more obvious concentrated structure aligning with the maxima peak. To date, except for the confirmed alignment phenomenon during the outburst of XTE J1810-197 (Woods et al. 2008), the alignment trend found in other magnetar reports during flux enhancement has been found to be inconclusive after in-depth study (Göğüş et al. 2017). According to Elenbaas et al. (2018) simulations, burst phase dependence is often affected by a number of external factors,

such as observer angle and the location of the radiation area, beam bunching, and also requires a sufficient number of bursts to ensure complete sampling. When the burst aligns near the maximum of the X-ray pulse profile, if it is a thermal burst, it may be generated from the surface of the neutron star. However, neither the capture of plasma fireball nor the hot spot generated by the bombardment of charged particles on the surface can explain the cause of the burst. It is possible that the thermal spectrum burst is generated by other different mechanisms at similar locations. If the observed phase alignment trend for non-thermal spectrum burst is true and not caused by observational effects or gravitational refraction, then it seems likely that the presence of a plasma fireball can explain this phenomenon, due to the twisted magnetic field the self-induction electric field lifts particles off the magnetar surface, accelerates them, and produces radiation. The rising particles are trapped in the magnetosphere, forming a corona of plasma that heats the star's surface and creates thermal radiation, which may coincide in phase. However, only our observational data now cannot derive a definite conclusion, and we need more high-quality data to carry out further research.

Acknowledgments

This work was partially supported by International Partnership Program of Chinese Academy of Sciences (Grant No.113111KYSB20190020) and by the National Key R&D Program of China (2021YFA0718500) from the Minister of Science and Technology of China (MOST). The authors thank supports from the National Natural Science Foundation of China under Grants U1938109, U1838201, U1838202, 12173103, U2038101, U1938103, 12133007, U1938201 and 11733009.

ORCID iDs

Xue-Feng Lu  <https://orcid.org/0000-0003-1272-3997>
 Li-Ming Song  <https://orcid.org/0000-0003-0274-3396>
 You-Li Tuo  <https://orcid.org/0000-0003-3127-0110>

References

- Bochenek, C. D., Ravi, V., Belov, K. V., et al. 2020, *Natur*, **587**, 59
 Borghese, A., Coti Zelati, F., Rea, N., et al. 2020, *ApJL*, **902**, L2
 Buccheri, R., Bennett, K., Bignami, G. F., et al. 1983, *A&A*, **128**, 245
 Cai, C., Xue, W.-C., Li, C.-K., et al. 2022a, *ApJS*, **260**, 24
 Cai, C., Xiong, S.-L., Lin, L., et al. 2022b, *ApJS*, **260**, 25
 Cao, X., Jiang, W., Meng, B., et al. 2020, *SCPMA*, **63**, 249504
 Chen, Y., Cui, W., Li, W., et al. 2020, *SCPMA*, **63**, 249505
 CHIME/FRB Collaboration, Andersen, B. C., Bandura, K. M., et al. 2020, *Natur*, **587**, 54
 Elenbaas, C., Watts, A., & Huppenkothen, D. 2018, *MNRAS*, **476**, 1271
 Ge, M., Yang, Y.-P., Lu, F., et al. 2022, arXiv:2211.03246
 Göğüş, E., Lin, L., Roberts, O. J., et al. 2017, *ApJ*, **835**, 68
 Israel, G. L., Esposito, P., Rea, N., et al. 2016, *MNRAS*, **457**, 3448
 Kaneko, Y., Göğüş, E., Baring, M. G., et al. 2021, *ApJL*, **916**, L7
 Kaspi, V. M., & Beloborodov, A. M. 2017, *ARA&A*, **55**, 261
 Kothes, R., Sun, X., Gaensler, B., & Reich, W. 2018, *ApJ*, **852**, 54
 Kouveliotou, C., Dieters, S., Strohmayer, T., et al. 1998, *Natur*, **393**, 235
 Li, C. K., Lin, L., Xiong, S. L., et al. 2021, *NatAs*, **5**, 378
 Lin, L., Göğüş, E., Roberts, O. J., et al. 2020a, *ApJL*, **902**, L43
 Lin, L., Göğüş, E., Roberts, O. J., et al. 2020b, *ApJ*, **893**, 156
 Liu, C., Zhang, Y., Li, X., et al. 2020, *SCPMA*, **63**, 249503
 Mereghetti, S., Savchenko, V., Ferrigno, C., et al. 2020, *ApJL*, **898**, L29
 Ridnaia, A., Svinkin, D., Frederiks, D., et al. 2021, *NatAs*, **5**, 372
 Scargle, J. D., Norris, J. P., Jackson, B., & Chiang, J. 2013, *ApJ*, **764**, 167
 Scholz, P., & Kaspi, V. 2011, *ApJ*, **739**, 12
 Stamatikos, M., Malesani, D., Page, K. L., & Sakamoto, T. 2014, *GCN*, **16520**, 1
 Thompson, C., & Duncan, R. C. 1995, *MNRAS*, **275**, 255
 Woods, P., Kouveliotou, C., Gavriil, F., et al. 2008, *ApJ*, **629**, 985
 Younes, G., Baring, M. G., Kouveliotou, C., et al. 2021, *NatAs*, **5**, 408
 Younes, G., Güver, T., Kouveliotou, C., et al. 2020, *ApJL*, **904**, L21
 Younes, G., Kouveliotou, C., Van der Horst, A. J., et al. 2017, *ApJ*, **847**, 15
 Zhang, S.-N., Li, T., Lu, F., et al. 2020, *SCPMA*, **63**, 249502